All-Solid-State Flexible Asymmetric Supercapacitor with Good Cycling Performance and Ultra-Power Density by Electrode Materials of Core-Shell CoNiO$_2$@NiAl-Layered Double Hydroxide and Hollow Spherical α-Fe$_2$O$_3$

Jijun Zhang [iD], Zexiang Chen[*], Yan Wang[*], Xinyu Yan, Zhiyu Zhou and Huifang Lv

Abstract

High electrochemical performance of asymmetric supercapacitor (ASC) depends on exquisite nanostructure design and synthesis of electrodes, including structural controllable design and synthesis of high theoretical performance materials and nanocomposite materials. Herein, a template-free hierarchical core-shell nanostructure of CoNiO$_2$@NiAl-layered double hydroxide (NiAl-LDH) and α-Fe$_2$O$_3$ with a hollow spherical structure composed of nanoparticles are successfully prepared. The CoNiO$_2$@NiAl-LDH as the cathode electrode and the hollow spherical α-Fe$_2$O$_3$ as the anode electrode of the ASC devices exhibit superior electrochemical performance. The gel of polyvinyl alcohol (PVA) and KOH acts as the solid electrolyte and the separator to assemble into the all-solid-state flexible ASC devices. Two of the CoNiO$_2$@NiAl-LDH//α-Fe$_2$O$_3$ ASC devices in series are fabricated to meet the voltage requirement of mobile energy equipment, which exhibit a maximum energy density of 65.68 Wh kg^{-1} at the power density of 369.45 W kg^{-1}. Interestingly, in addition to many advantages that the solid electrolyte in ASC devices already have, we find that it can be an alternative way of solving the problem of iron oxide cycling performance, and of course it can also be used as a reference for other materials with poor cycling performance.

Keywords: Asymmetric supercapacitors, Rate capability, CoNiO$_2$, NiAl-LDH, α-Fe$_2$O$_3$, State electrolyte

Introduction

With the development of electric vehicles, traditional energy storage equipment has been difficult to meet the demand of high-energy density and high-power density. Although lithium-ion battery has high energy density, its intrinsic factors limit its power density, which is hard to meet the requirement of the output of high power in practical application of electric vehicle. Supercapacitor is the energy storage device between dielectric capacitor and rechargeable battery exhibiting fast charge-discharge rate, high power density, low cost and good cycling stability, etc. [1–5]. Supercapacitors can fall into two diverse types by the energy storage mechanism, one is the electrical double-layer capacitors (EDLCs), dominated by the adsorption and desorption of the electrostatic charge in the interface and have high power density and stable cycling characteristics but possess limited energy density; the other is pseudocapacitors, also called Faraday capacitor which is dominated by the Faradaic redox reaction and have considerable energy density [6]. The electrode materials of EDLCs generally consist of carbon materials, such as activated carbon [7], activated carbon fiber [8], carbon nanotubes [9], and graphene [10]. While the electrode materials of the pseudocapacitors are often composed of transition metal oxides, transition metal hydroxides, or layer double hydroxides, such as RuO$_2$

* Correspondence: zxchen@uestc.edu.cn; wangyan127@uestc.edu.cn
School of Optoelectronic Science And Engineering, University of Electronic Science and Technology of China, North Jianshe Road 4, Chengdu 610054, China

[11], NiO [12], Mn_2O_3 [13], MnO_2 [14], Co_3O_4 [15], $NiCo_2O_4$ [16], $CoNiO_2$ [17], $Ni(OH)_2$ [18], $Co(OH)_2$ [19], NiAl-layered double hydroxide (NiAl-LDH) [20], NiCo-LDH [21], CoAl-LDH [22], and so on. One of the big obstacles to limiting the practical use of supercapacitors is that they have a much smaller energy density than the secondary battery. Generally, in the same specific surface area, the pseudocapacitors can provide more than ten times storage capacity than the electric double-layer capacitance which have attracted great interest in increasing their energy densities of the pseudocapacitors to partially replace the current commercialized two-time battery. However, the pseudocapacitors suffer from the low conductivity of active materials with poor power characteristics and poor cyclic stability caused by volumetric expansion during the charge and discharge processes.

In recent years, the pseudocapacitors have received considerable progress, especially in their energy density [23–26]. The oxidized nickel-based layered double hydroxides (LDHs), also known as anionic clays, have drawn intensive attention as pseudocapacitive cathode materials because of their high theoretical capacitance, stable cycling performance, abundance in the earth, and environmentally friendly [27, 28]. However, one of the main disadvantages of LDHs is the poor conductivity, which limits their power density and the application in high-power devices in the future. For solving this problem, there is a growing number of research on the complex heterostructure nanomaterials of LDHs such as NiAl-LDHs on Ni foam [29], NiAl-LDHs@carbon nanoparticles [30], NiMn-LDHs/carbon nanotubes [31], $NiCo_2S_4$ Nanotube@NiMn LDHs [32], NiCoAl-LDH/NiCo-Carbonate hydroxide [33], NiAl-LDHs/graphene [34], and so on. Some of the above-mentioned studies have indeed increased their conductivity than individual material, but due to the introduction of conductive medias or other active materials, the energy densities of the overall active materials have a certain effect. Therefore, to find a material which has a good conductivity and can also provide a relatively better energy density to compound with LDHs is critical for LDH materials.

Many efforts have been done to focus on the anode materials of the pseudocapacitors to achieve high capacity and good cyclic behavior, including RuO_2 [35], FeO_x [36–38], ZnO [39], VO_x [40–42], and so on. Among them, $\alpha\text{-}Fe_2O_3$ is a promising anode material which has attracted great deal of research interest due to the appropriate potential window for rich redox chemistry, the high theoretical capacity, the relatively stable structure, low cost, and abundance in the earth. In recent advance, the reported capacity and the cycling stability of $\alpha\text{-}Fe_2O_3$ is far below its theoretical capacity and a long way from commercial use, respectively, which can

be contributed to the poor conductivity, the reduction of the active regions, and the volume changes of the electrodes during the redox reaction. In order to address these challenges, researchers have developed different nanostructures of $\alpha\text{-}Fe_2O_3$ for improvement of electrochemical properties, which can be categorized as nanowires, nanotubes, nanosheets, nanosphere, and nanoflowers. But for all this, the transformation of crystal structure of the $\alpha\text{-}Fe_2O_3$ is occurred in the redox reaction, which will lead to the volume changes and the reduction of the active regions. It still restrains the utilization of $\alpha\text{-}Fe_2O_3$ in the anode of the supercapacitors. Therefore, it is very urgent to find an effective way to develop $\alpha\text{-}Fe_2O_3$ as the anode electrode of supercapacitors with both high specific capacity and good cycling performance.

Based on the above consideration, we report a hierarchical $CoNiO_2$@NiAl-LDHs core-shell nanosheet as the cathode electrode and the hollow sphere of $\alpha\text{-}Fe_2O_3$ as the anode electrode of all-solid-state supercapacitor, which PVA&KOH was introduced as the solid electrolyte and separator. $CoNiO_2$ is a kind of nickel-cobalt material oxides, which has been confirmed that it is a material with high energy density and good conductivity in our previous research work [17]. $CoNiO_2$ was constructed as an inner framework for supporting the outer shell of NiAl-LDHs nanosheets. Two kinds of materials in the inside and outside are based on the nickel element as the main framework, making it easy to form a whole integrated architecture. The structure of $CoNiO_2$@-NiAl-LDHs effectively reduced the contact resistance and further increased the effective active area of NiAl-LDHs. The unique 3D hollow sphere of $\alpha\text{-}Fe_2O_3$ is made up of nanoparticles, which enables each nanoparticle to be easily in contact with the all-solid-state electrolyte and provides sufficient active region for electrochemical reactions. The as-prepared $CoNiO_2$@-NiAl-LDHs cathode electrode exhibited a high specific capacitance of 1905 F g^{-1} at the current density of 1 A g^{-1}. And even at the current density of 8 A g^{-1}, the specific capacitance can be maintained at 1555 F g^{-1}. Meanwhile, the hollow sphere of $\alpha\text{-}Fe_2O_3$ anode electrode displayed a remarkable electrochemical performance, which the specific capacitance can achieve 802 F g^{-1} at 1 A g^{-1} and 70.3% of the capacity retention with the high current density of 16 A g^{-1}. Two all-solid-state asymmetric supercapacitor (ASC) devices in series are assembled by the cathode electrode material of $CoNiO_2$@NiAl-LDHs and the anode electrode material of $\alpha\text{-}Fe_2O_3$ with the electrolyte of PVA&KOH, which exhibits a maximum energy density of 65.68 Wh kg^{-1} at the power density of 369.45 W kg^{-1}. Moreover, the system shows a prominent cycling stability of 88.8% retained over 1000 cycles at 1 A g^{-1}.

Zhang *et al. Nanoscale Research Letters* (2019) 14:87

Page 3 of 11

Methods

Materials

All the reagents were of analytical grade without any further purification. Nickel nitrate hexahydrate ($Ni(NO_3)_2 \cdot 6H_2O$), cobalt nitrate hexahydrate ($Co(NO_3)_2 \cdot 6H_2O$), aluminum nitrate nonahydrate ($Al(NO_3)_3 \cdot 9H_2O$), Iron(III) chloride hexahydrate ($FeCl_3 \cdot 6H_2O$), anhydrous ethanol, and hexadecyl trimethyl ammonium bromide (CTAB) were obtained from Sinopharm Chemical Reagent Co. Sodium-p-styrenesulfonate (PSS) was gained from Aladdin Chemical Reagent Co.

Preparation of the PVA&KOH

In a typical preparation of PVA&KOH, 6 g polyvinyl alcohol (PVA) was added to the 40 ml deionized water and was heated to 95 °C for 2 h with magnetic stirring. And then 4 g KOH was dissolved in 10 ml deionized water. The obtained KOH solution was added to the PVA solution dropwise. After that, continued stirring for 30 min and cooled down to the temperature of 30 °C. Finally, the PVA&KOH was formed.

Synthesis of CoNiO2

In a typical synthesis procedure, firstly, the $Ni(NO_3)_2 \cdot 6H_2O$ and $Co(NO_3)_2 \cdot 6H_2O$ solution of 1 mol L^{-1} were prepared, respectively. And then 4 ml of $Ni(NO_3)_2 \cdot 6H_2O$ and 4 ml $Co(NO_3)_2 \cdot 6H_2O$ were added into 32 ml deionized water with magnetic stirring for 10 min, followed by 0.12 g PSS was dissolved in the solution with magnetic stirring for 15 min. In addition, the 36 mmol of urea was poured into the above solution with continuous magnetic stirring for 15 min. The resulting transparent solution was poured into a 50 ml Teflon kettle with stainless steel autoclave for hydrothermal reaction at 90 °C for 12 h. After the reactor was cooled down to room temperature, the products were collected and washed by centrifugation and rinsed with deionized water and ethanol for several times, respectively. The obtained products of the $CoNiO_2$ precursors were dried at 60 °C for 12 h and calcinated at 300 °C in air atmosphere for 2 h at a heating rate of 5 °C min^{-1}.

Synthesis of CoNiO2@NiAl-LDHs

The NiAl-LDHs were grown on the prepared $CoNiO_2$ to form the $CoNiO_2$@NiAl-LDHs materials also by a hydrothermal method. Then, 0.2 g as-prepared $CoNiO_2$ and 1.2 g hexadecyl trimethyl ammonium bromide (CTAB) was dispersed in the solutions of 20 ml deionized and 20 ml ethanol with ultrasonic dissolution for 30 min and magnetic stirring for 20 min. Then, 3 mmol $Ni(NO_3)_2 \cdot 6H_2O$ and 1 mmol $Al(NO_3)_3 \cdot 9H_2O$ were added; the mixture kept under magnetic stirring for 10 min, followed by 16 mmol urea was added with magnetic stirring for 15 min. And then the obtained solution was transferred to a 50 ml Teflon kettle with stainless steel autoclave for hydrothermal reaction at 90 °C for 12 h. When the reactor cooled down to room temperature, the products were collected and washed by centrifugation with deionized water and ethanol for several times. And then the obtained products were dried at 60 °C for 12 h in air atmosphere.

Synthesis of α-Fe₂O₃

In a typical procedure, 10 mmol $FeCl_3 \cdot 6H_2O$ was dissolved into 40 ml of anhydrous ethanol and 40 ml deionized water with magnetic stirring for 30 min. The obtained transparent solution was transferred to a 100 ml Teflon kettle with stainless steel autoclave for hydrothermal reaction at 200 °C for 12 h. The products were collected and washed by centrifugation and rinsed with deionized water and ethanol for several times, respectively. And then the as-prepared products were also dried at 60 °C for 12 h in air atmosphere.

Characterization

The as-prepared materials were characterized by X-ray diffractometer (PANalytical X'Pert Pro XRD, CuKa λ = 0.15405 nm) with a scan rate of 5° min^{-1}. Morphology of the prepared products were examined by field emission scanning electron microscopy (FESEM, Inspect F, FEI) with accelerating voltage of 20 kV. Moreover, the transmission electron microscopy (TEM), the high-resolution transmission electron microscopy (HRTEM), and energy dispersive X-ray (EDX) spectroscopy data were acquired using an FEI Tecnai F20 electron microscope operated at accelerating voltage of 200 kV.

Electrochemical Measurements

Electrochemical tests were characterized in a three-electrode electrochemical system with an aqueous electrolyte solution of 6 M KOH. A platinum foil was served as the counter electrode, and the Hg/HgO electrode was served as a reference electrode. Ni foam (110 PPI, thickness: 1.5 mm, surface density: 380 g m^{-2}, Lizhiyuan Co., Ltd.) was cut to a size of 1×6 cm, washed with ethanol and deionized water in an ultrasonic bath, and used as a current collector. To prepare the working electrodes, sample powders, super-p, and polytetrafluoroethylene (PTFE) were combined in the mass ratio of 80:15:5 in a small amount of ethanol and formed into a homogeneous paste. The paste was then painted on Ni foam (1 cm × 1 cm) and pressed into an anode electrode sheet using hydraulic pressing at a temperature of 150 °C after drying at 80 °C in air. The mass loading of the cathode electrode and the anode electrode were about 20 mg cm^{-2}, respectively. Electrochemical tests were carried out by an RST5200F electrochemical workstation (Suzhou Risetest Electronic Co., Ltd., Suzhou, China).

Zhang *et al. Nanoscale Research Letters* (2019) 14:87

Page 4 of 11

The values of specific capacitance for the working electrodes were calculated by the following formula (1):

$$C = I\Delta t / m\Delta V \qquad (1)$$

The symbols of *C*, *I*, Δ*t*, *m*, Δ*V* represent the specific capacitance (F g^{-1}) of the active material of the electrode, discharge current (A), discharge time (s), the mass loading of the active material (g), the potential window of discharge (V), respectively. In addition, the electrochemical impedance spectroscopy (EIS) was carried out with the AC voltage of 5 mV amplitude in the frequency range of 0.01 Hz–10 kHz at the open circuit potential.

Results and Discussion

The schematic fabrication process is displayed in Fig. 1. Firstly, CoNiO$_2$ was prepared using a hydrothermal method followed by a calcining process. And then CTAB and the CoNiO$_2$ were mixed together in deionized water by stirring and ultrasonic. Subsequently, the CoNiO$_2$@NiAl-LDH was obtained by another hydrothermal reaction. Meanwhile, the hollow sphere of α-Fe$_2$O$_3$ was grown by a hydrothermal way. The all-solid-state ASC device was fabricated by the CoNiO2@NiAl-LDH as the cathode material, the α-Fe$_2$O$_3$ as the anode material, the foamed nickel as the current collect collector, and the PVA&KOH as the electrolyte and the separator.

The phase and composition of the samples are illustrated by X-ray diffraction (XRD) presented in Fig. 2a. The sharp peaks for the resultant CoNiO$_2$ locate at 36.8°, 42.8°, 61.8°, 74.0°, and 80.0° are indexed to CoNiO$_2$

(JCPDS Card no. 10-0188). And all the diffraction peaks of the resultant NiAl-LDH are in good agreement with the phase of Ni$_5$Al$_4$O$_{11}$·18H$_2$O (JCDPS Card no. 22-0452). After the hydrothermal growth of the NiAl-LDH, the XRD pattern of the hybrid structure (green line) contains the peaks of CoNiO$_2$ and NiAl-LDH, revealing that the two phases of the obtained NiAl-LDH are coexistent on the surface of CoNiO$_2$. In the hybrid structure, the intensity of the diffraction peaks relative to the CoNiO$_2$ decreases, which is likely that the NiAl-LDH is distributed on the surface of CoNiO$_2$ nanostructure and concealed by the strong diffraction peaks of the NiAl-LDH. Figure 2b, c presents the SEM images of the as-synthesized CoNiO$_2$ and CoNiO$_2$@NiAl-LDH, which reveal that the CoNiO$_2$ with a diameter of approximately 40 nm were interlaced with each other to construct a three-dimensional structure and facilitate the transport of electrons inside of active materials. Compared with the CoNiO$_2$, the NiAl-LDH nanosheets were grown on the surface of the CoNiO$_2$ to form the CoNiO$_2$@NiAl-LDH with a diameter of approximately 100 nm as shown in Fig. 2c which the interconnected nanosheets may promote the efficient contact of electrolyte ions. It can be seen from the TEM image in Fig. 2d that the diameter of CoNiO$_2$@NiAl-LDH is mainly consistent with that obtained by the SEM images. Meanwhile, in Fig. 2d, the nanosheets can be clearly observed; however, the framework of CoNiO$_2$ is hard to find, which probably the CoNiO$_2$ recrystallized and combined with NiAl-LDH during the hydrothermal reaction of growing NiAl-LDH. The interplanar spacings is
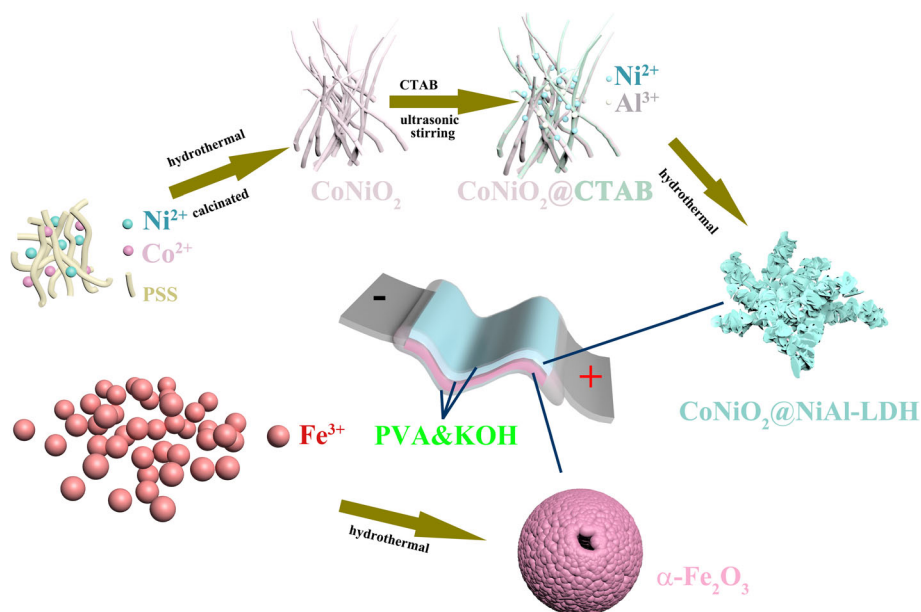

Fig. 1 Schematic illustration of the synthesis procedure for CoNiO$_2$@NiAl-LDH, the hollow sphere of α-Fe$_2$O$_3$, and the formed solid ASC device with the electrolyte of PVA&KOH
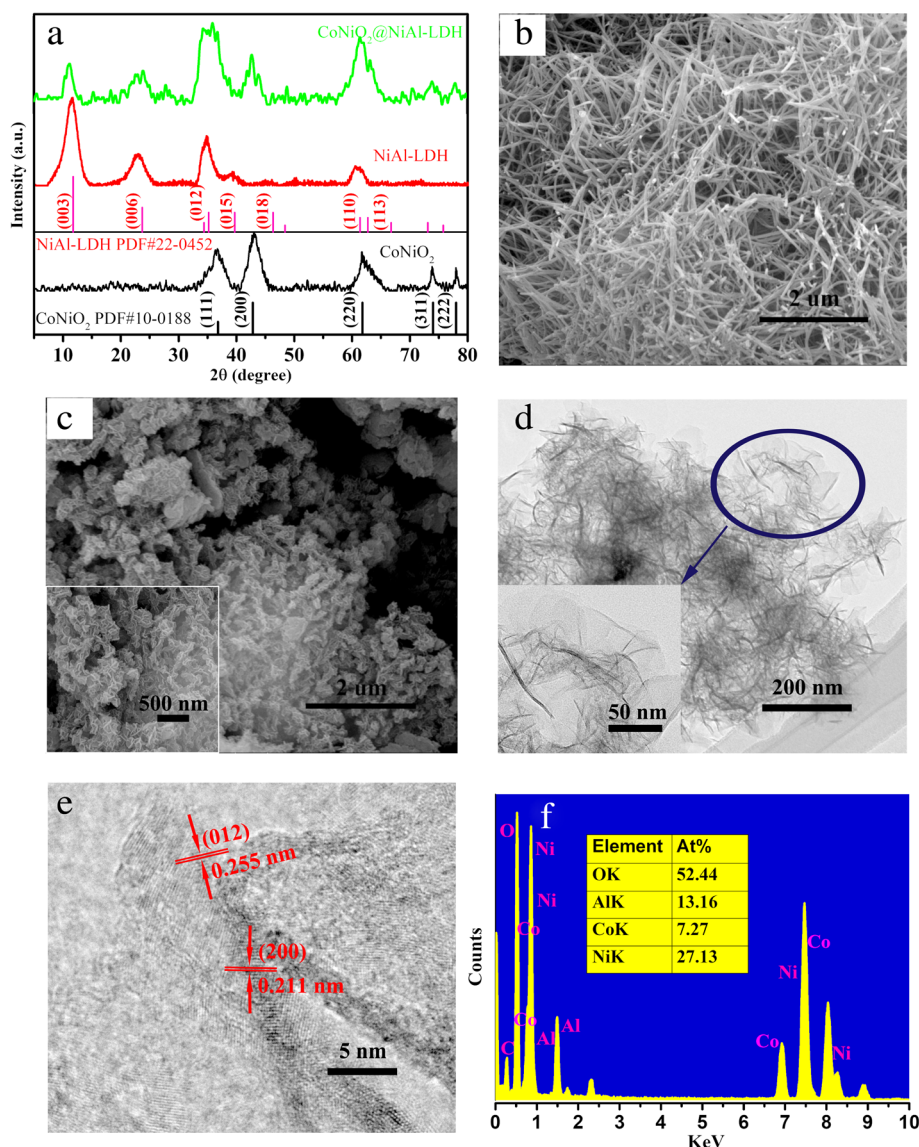
Fig. 2 a XRD patterns of samples: CoNiO₂, NiAl-LDH, CoNiO₂@NiAl-LDH. **b, c** SEM image of CoNiO₂, CoNiO₂@NiAl-LDH. **d** TEM images of CoNiO₂@NiAl-LDH. **e** TEM images at high magnifications. **f** The EDX spectrum of the CoNiO₂@NiAl-LDH

displayed in the high-resolution TEM (HRTEM) images in Fig. 2e, which the measured values are 0.211 nm and 0.255 nm, corresponding to (200) planes of $CoNiO_2$ and (012) planes of NiAl-LDH, respectively. Figure 2f shows the energy dispersive X-ray (EDX) that indicates the existence of O, Al, Co, and Ni elements, which the atomic ratio is corresponding well with the atomic ratio of the CoNiO₂@NiAl-LDH.

The as-synthesized hollow sphere α-Fe_2O_3 is characterized by powder XRD analysis, as observed in Fig. 3a. The distinct diffraction peaks are detected at 2θ values of 24.1°, 33.2°, 35.6°, 40.8°, 49.5°, 54.1°, 57.6°, 62.4°, 64.0°, 71.9°, and 75.4°, which can be indexed to (012), (104), (110), (113), (024), (116), (018), (214), (300), (1010), and

(220) plane reflections of the hematite (α-Fe_2O_3 JCPDS Card no. 33-0664). No other peaks are detected from possible impurities, such as the diffraction peaks of Fe_3O_4, FeOOH, or γ-Fe_2O_3, which indicates that the as-prepared hollow sphere α-Fe_2O_3 has a high purity. Morphological features of as-prepared α-Fe_2O_3 are studied by SEM and TEM as illustrated in Fig. 3b–d. It is evident that the diameter of the hollow sphere α-Fe_2O_3 is approximately 1.5 μm from Fig. 3b. Further observation finds that the hollow sphere α-Fe_2O_3 is made up of nanoparticles with an average size of 70–80 nm which is also clearly observed from the edge of the as-prepared α-Fe_2O_3 in the TEM images of Fig. 3c. The high resolution of the TEM images shows the interplanar spacing
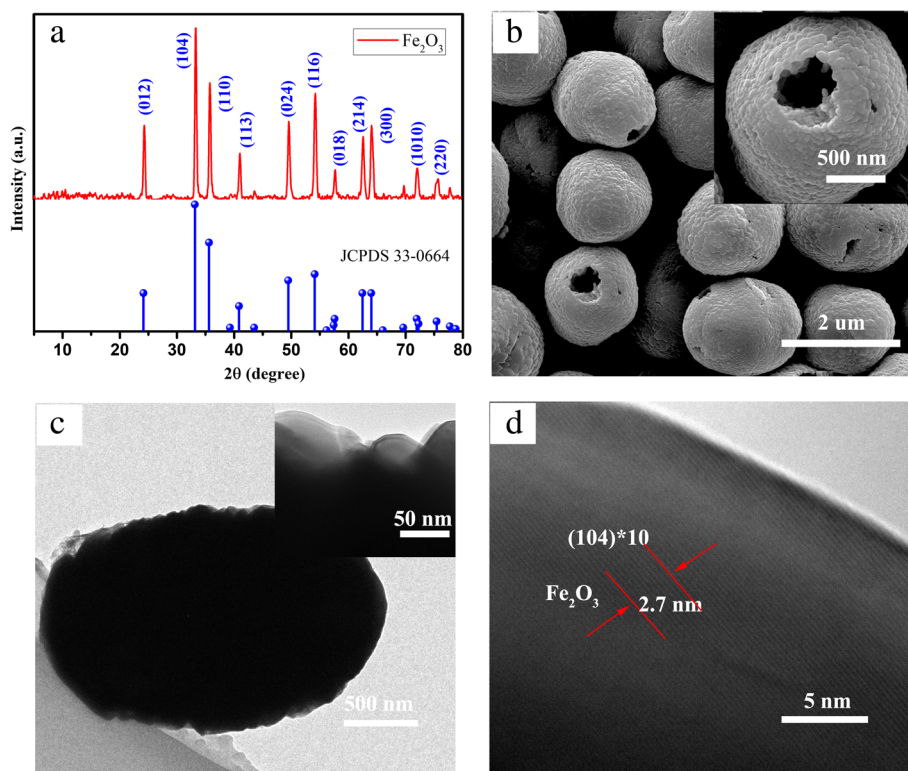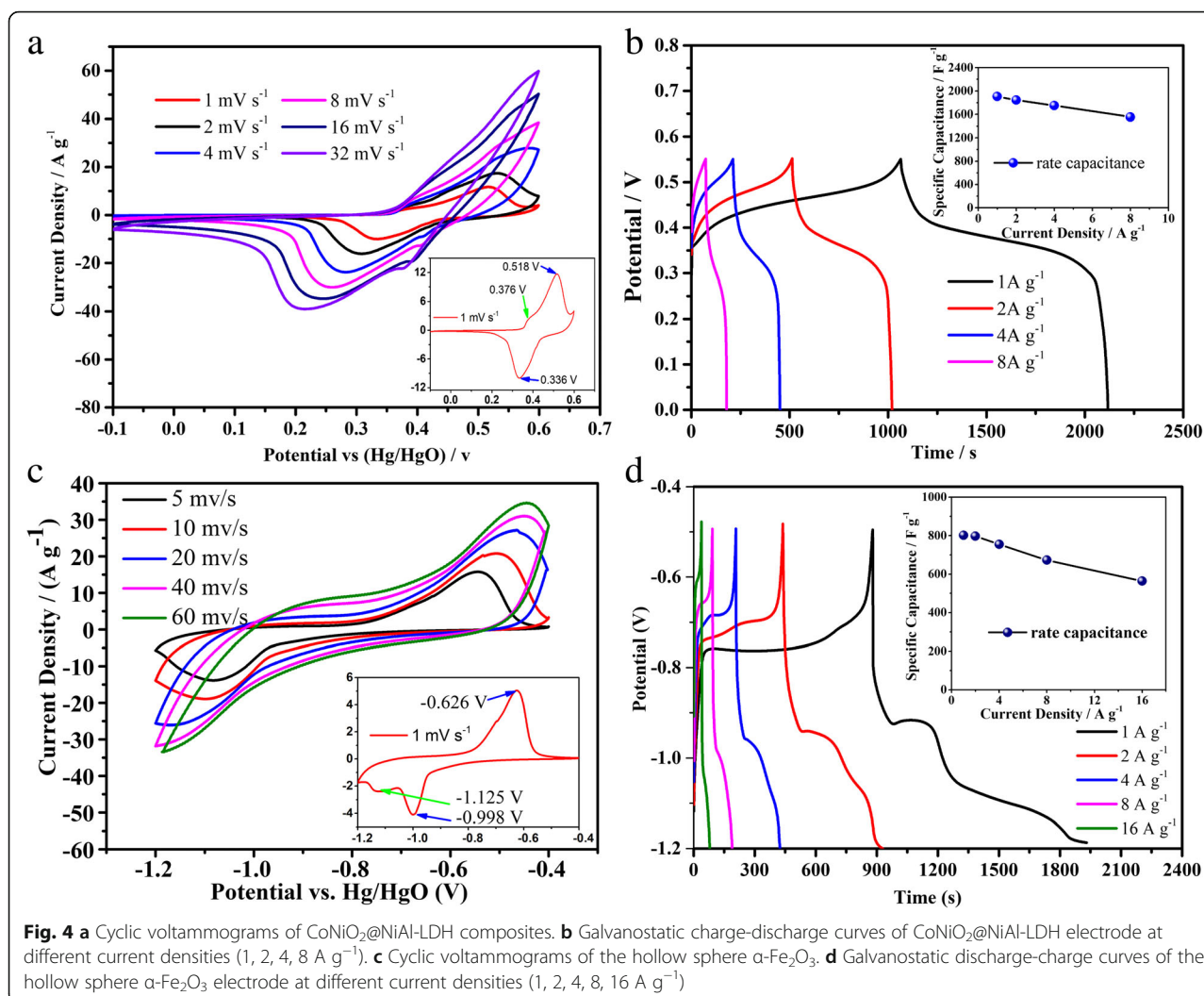
Zhang *et al. Nanoscale Research Letters* (2019) 14:87

Page 6 of 11

Fig. 3 a XRD pattern of samples: α-Fe2O3. **b** SEM image of α-Fe$_2$O$_3$. **c** TEM images of α-Fe$_2$O$_3$. **d** TEM images at high resolution

of the hollow sphere α-Fe$_2$O$_3$, as observed in Fig. 3d, which the measured value is 0.27 nm, corresponding to (104) plane of α-Fe$_2$O$_3$.

To evaluate the electrochemical characteristics of CoNiO$_2$@NiAl-LDH and α-Fe$_2$O$_3$ as electrode materials, the electrochemical tests are performed in a three-electrode system in 6 M KOH aqueous electrolyte, which the Hg/HgO and Pt are employed as the reference electrode and the counter electrode, respectively. Figure 4a shows the CV curves of CoNiO$_2$@NiAl-LDH electrode at the scan rate of 1, 2, 4, 8, 16, and 32 mV s^{-1} in the potential window of – 0.1 to 0.6 V (vs. Hg/HgO). It can be found that the CV curves at different scan rate basically share a similar shape, whereas with the increase of the scan rate, the oxidation peaks slowly shift toward the positive voltage and the reduction peaks slowly shift toward the negative voltage, attributed to the polarization effect of the electrode [5]. The peak are merely shifted by 0.11 V when the scan rate is increased from 1 to 32 mV s^{-1}, indicating a low resistance of the CoNiO$_2$@NiAl-LDH electrode. Meanwhile, with the increase of the scan rate, the peak current increases, implying the rapid electron and ion transfer rates. The CV curve is exhibited at the scan rate of 1 mV s^{-1} in the bottom-right side of Fig. 4a. It is evident that some of redox peaks were observed, such as the oxidation peak at 0.518 V and the reduction peak at 0.336 V, which is

primarily due to the redox reaction of the Ni [43]. Meanwhile, the oxidation peak at 0.378 V was also detected in the CV measurements, implying that the Co specie also plays a role in the redox reaction at the scan rate of 1 mV s^{-1}. However, with the increase of the scan rate, the oxidation peak of Co is disappeared, which indicates that the Co specie may exist mainly as a conducting medium in the nanocomposites of CoNiO$_2$@NiAl-LDH.

The galvanostatic charge-discharge measurements of CoNiO$_2$@NiAl-LDH electrode is conducted at the current densities of 1 A g^{-1}, 2 A g^{-1}, 4 A g^{-1}, and 8 A g^{-1} with a potential window between 0 and 0.55 V (vs Hg/HgO), as presented in Fig. 4b. There is a distinct platform region during the charge and discharge, which suggests the faradaic pseudocapacitive behavior of the electrodes. At the same current densities, the specific capacitances are calculated by the formula (1), as shown in the top-right side of Fig. 4b, which exhibits a high specific capacitance of 1905 F g^{-1} at the current density of 1 A g^{-1} and much larger than our former research of CoNiO$_2$ (1462 F g^{-1}) [17] and NiAl-LDH (1313 F g^{-1}) [44]. The specific capacitance retention is up to 81.6% at the current density of 8 A g^{-1}, implying the electrode of CoNiO$_2$@NiAl-LDH has an excellent rate capability and it can be attributed to the core-shell nanostructure. The outstanding electrochemical performance of CoNiO$_2$@-NiAl-LDH is better than most of previously reported for

Fig. 4 a Cyclic voltammograms of CoNiO₂@NiAl-LDH composites. **b** Galvanostatic charge-discharge curves of CoNiO₂@NiAl-LDH electrode at different current densities (1, 2, 4, 8 A g^{-1}). **c** Cyclic voltammograms of the hollow sphere α-Fe₂O₃. **d** Galvanostatic discharge-charge curves of the hollow sphere α-Fe₂O₃ electrode at different current densities (1, 2, 4, 8, 16 A g^{-1})

bimetallic oxides and the layer double hydroxides, especially the high discharge voltage plateau, such as NiCo₂O₄@MnMoO₄ [45], NiP@CoNi-LDH [46], NiCo-LDH/NiCoP@NiMn-LDH [47], MnCo₂O₄@Co₃O₄ [48], and so on.

The CV curves of the as-prepared α-Fe₂O₃ are measured at the scan rate of 5, 10, 20, 40, and 60 mV s^{-1} in the potential window of − 1.2 to − 0.4 V (vs. Hg/HgO) in Fig. 4c. It can be seen that the CV curves also share a similar shape with a pair of the oxidation peak and the reduction peak, indicating the behavior of the pseudocapacitance. The oxidation peak are only just shifted by 0.1 V when the scan rate is increased from 5 to 60 mV s^{-1}, implying a very low resistance of the as-prepared α-Fe₂O₃ electrode. The CV curve with a slow scan rate of 1 mV s^{-1} is displayed in the bottom-right side of Fig. 4c. It can be observed that the oxidation peak is − 0.626 V and the reduction peak is − 0.998 V, corresponding to the conversion between Fe^{3+} and Fe^{2+} [49]. But at the same time, the reduction peak

of − 1.125 V is also observed, which probably some of the materials involved in the conversion between Fe^{3+} and Fe [50].

The galvanostatic discharge-charge tests of α-Fe₂O₃ electrode is carried out at the current densities of 1 A g^{-1}, 2 A g^{-1}, 4 A g^{-1}, 8 A g^{-1}, and 16 A g^{-1} with a potential window between − 0.1 and − 1.2 V (vs Hg/HgO), as presented in Fig. 4d. It can be also found that a distinct platform region is occurred during the charge and discharge, indicating the faradaic pseudocapacitive behavior of the as-prepared α-Fe₂O₃ electrodes. The specific capacitances are calculated at the current density of 1, 2, 4, 8, and 16 A g^{-1}, as shown in the top-right side of Fig. 4d. The specific capacitance of 1 A g^{-1} is 802 F g^{-1} and only 29.7% loss of the capacitance is acquired at the current density of 16 A g^{-1}, where the rate capability is higher than that of Fe₂O₃ based on previous work [51–55].

The assembly schematic two solid ASC devices in series (named as TSASC) is shown in Fig. 5a. It can be seen that the foamed nickel is regarded as the current
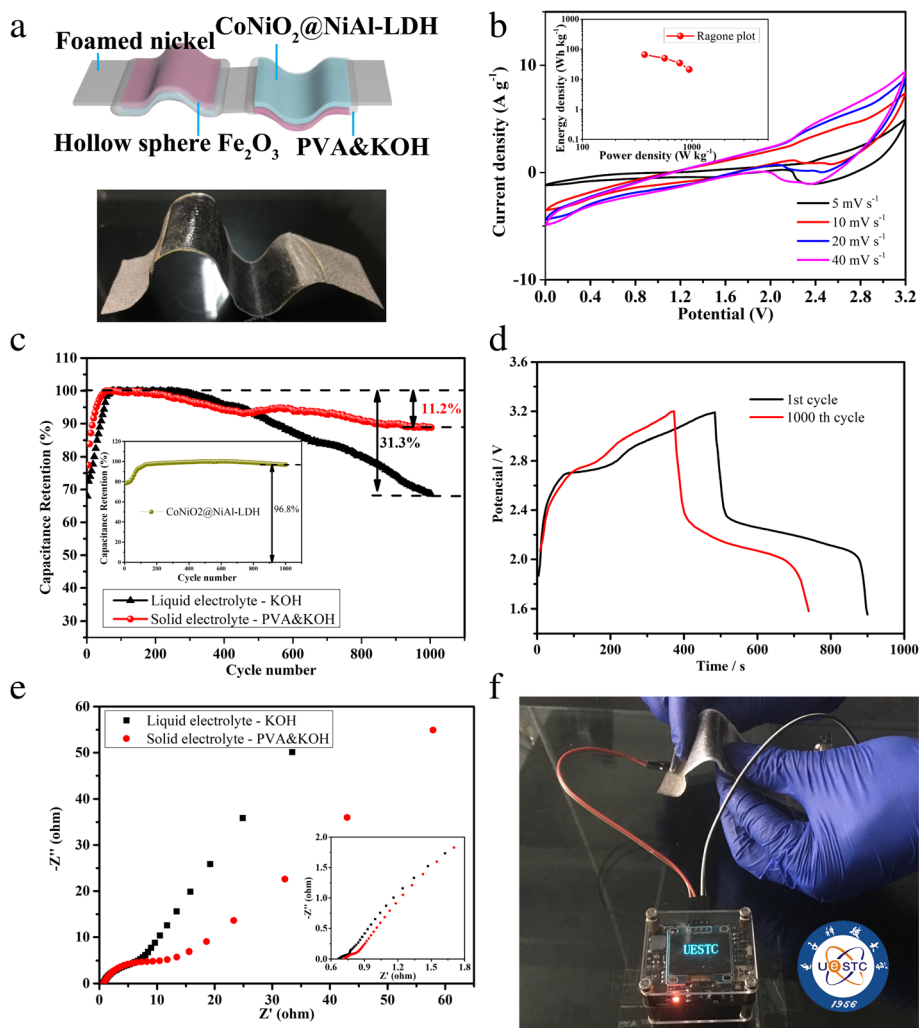
Fig. 5 a The assembly schematic of two solid ASC devices in series and photograph of the as-prepared two solid ASC devices in series. **b** Cyclic voltammograms of two solid CoNiO$_2$@NiAl-LDH/α-Fe$_2$O$_3$ in series and the ragone plots in the top-left side. **c** Cycling performance of the liquid ASC devices and the solid ASC devices of CoNiO$_2$@NiAl-LDH//α-Fe$_2$O$_3$ at the current density of 1 A g^{-1}. **d** The comparison of the galvanostatic charge-discharge measurements between the 1st and 1000th in 1 A g^{-1}. **e** The comparison of the Nyquist plots of the liquid ASC devices and the solid ASC devices. **f** Photograph of an OLED display powered by the two solid ASC in series

collector, the hollow sphere as the material of the anode electrode, the CoNiO$_2$@NiAl-LDH as the material of the cathode electrode, and the PVA&KOH as the separator and the solid electrolyte. In addition, only one foamed nickel (a cathode electrode at one end and an anode electrode at the other end of the nickel foam) is used as the connection part of TSASC, which can reduce the contact resistance at the junction of two electrodes. The photograph of the as-prepared TSASC is displayed in the bottom of Fig. 5a, implying a good flexibility of the devices.

The cyclic voltammograms of two solid CoNiO$_2$@-NiAl-LDH//α-Fe$_2$O$_3$ in series are conducted at the scan rate of 5 mV s^{-1}, 10 mV s^{-1}, 20 mV s^{-1}, and 40 mV s^{-1} with the potential window between 0 and 3.2 V, as shown in Fig. 5b. It can be observed that the CV curves

share a similar shape and the position of redox peak is nearly no shift with the scan rates increased, suggesting a good rate capability of the ASC devices. And the Ragone plots of the two solid CoNiO$_2$@NiAl-LDH//α-Fe$_2$O$_3$ in series ASC devices are shown in the bottom of Fig. 4b which the power density and the energy density are calculated by the CV curves at the scan rate of 5 mV s^{-1}, 10 mV s^{-1}, 20 mV s^{-1}, and 40 mV s^{-1}. The CoNiO$_2$@NiAl-LDH//α-Fe$_2$O$_3$ TSASC devices exhibit a maximum energy density of 65.7 Wh kg^{-1} with the power density of 369.45 W kg^{-1} at the CV scan rate of 5 mV s^{-1} and even at the scan rate of 10 mV s^{-1}, the energy density can still be remained 21.1 Wh kg^{-1} with the power density of 946.35 W kg^{-1} based on the sum of the total mass of cathode and anode active substances,

Zhang *et al. Nanoscale Research Letters* (2019) 14:87

Page 9 of 11

indicating a considerable rate capability in the two all-solid state in series devices.

The electrochemical stabilities of the $CoNiO_2$@-NiAl-LDH//α-Fe_2O_3 TSASC devices and the two liquid $CoNiO_2$@NiAl-LDH//α-Fe_2O_3 in series ASC (named as TLASC) devices are evaluated by the galvanostatic charge-discharge measurements with the current density of 1 A g^{-1} for 1000 cycles, as shown in Fig. 5c. The $CoNiO_2$@NiAl-LDH//α-Fe_2O_3 TSASC devices exhibit remarkable cycling stability with 88.8% specific capacitance retention while the $CoNiO_2$@NiAl-LDH//α-Fe_2O_3 TLASC devices only achieve 68.7% after 1000 cycles. Additionally, the cycling stability of $CoNiO_2$@NiAl-LDH for the cathode materials is presented in the embedded chart of Fig. 5c, indicating an excellent cycling stability with 96.8% retention of the specific capacitance. That means the attenuation of cyclic performance for the ACS devices are mainly caused by the instability of the anode material of α-Fe_2O_3 in a continuous redox reaction [56]. Compared the cycling stability of TSASC and TLASC, it can be found that the solid electrolyte of PVA&KOH can increase the stability of the anode material of α-Fe_2O_3, which can be probably that the solid electrolyte of PVA&KOH limits the expansion and passivation of α-Fe_2O_3 during the continuous redox reaction. It is equivalent to solving the problem of iron oxide cycling performance in an alternative way, and of course it can be analogue to other materials with poor cycling performance.

The comparison of galvanostatic charge-discharge tests with the current density of 1 A g^{-1} between the origin cycle and 1000th cycle is presented in Fig. 4d. It can be seen that both of two galvanostatic charge-discharge curves have charging and discharging platforms, suggesting a Faradaic reaction. The discharge platform of the 1st cycle is higher than that of the 1000th cycle and the discharge time of the 1st cycle is longer than that of 1000th cycle, which indicates that the electrode materials still have a certain degree of passivation, although the PVA&KOH can prevent some passivation of the electrode materials. Meanwhile, the charge platform of the 1000th cycle is higher than that of the 1st cycle, implying the increase of the internal resistance of the ASC devices.

Further studying the electrochemical properties of the $CoNiO_2$@NiAl-LDH//α-Fe_2O_3 TLASC and TSASC devices, the electrochemical impedance (EIS) is carried out at the open circuit potential. Figure 5e shows the Nyquist plots of the $CoNiO_2$@NiAl-LDH//α-Fe_2O_3 TLASC and TSASC devices in the frequency range of 0.01 Hz to 100 kHz with an AC perturbation of 5 mV. The Nyquist plots can be divided into two distinct parts of a semicircle in the high-frequency region and a straight line in the low-frequency region. And the intercepts of the Nyquist plots on the real axis are about 0.67 and 0.72 Ω for the $CoNiO_2$@NiAl-LDH//α-Fe_2O_3

TLASC and TSASC, respectively, indicating the extremely low intrinsic resistances. The intrinsic resistances are lower than most of previous reported Fe_2O_3-based ASC devices [57–60]. Comparing to the Nyquist plots of $CoNiO_2$@NiAl-LDH//α-Fe_2O_3 TLASC and TSASC, it can be found that the small semicircle diameter of the TSASC is larger than that of TLASC, suggesting that the solid electrolyte of PVA&KOH has a certain barrier for electron transportation. It is proved that the conductivity of one-dimensional nanostructures is better than that of bulk materials [37]. The interlaced nanowires of $CoNiO_2$ can act as the channel for efficient electron transportation between the NiAl-LDH and the current collectors and the hollow sphere structure of α-Fe_2O_3, composed of nanoparticles, also possesses good conductivity and the ability to efficient transport electron. It is the reason that the Nyquist plots shows low intrinsic resistances and good charge-transfer abilities. An organic light-emitting diode (OLED) display with drive circuit is used to simulate the application of the $CoNiO_2$@NiAl-LDH//α-Fe_2O_3 TSASC on the mobile phone, which the TSASC successfully powered the OLED display and the brightness of the screen is very high as shown in Fig. 5e.

Conclusion

In summary, a template-free hierarchical nanostructure $CoNiO_2$@NiAl-LDH nanocomposite and α-Fe_2O_3 with a hollow spherical structure composed of nanoparticles were successfully prepared. The cathode electrode of $CoNiO_2$@NiAl-LDH exhibits outstanding electrochemical performance with a high specific capacitance of 1905 F g^{-1} at 1 A g^{-1} and also possesses 1555 F g^{-1} (81.6% of initial capacitance) at the high current density of 8 A g^{-1}, implying a good rate capability, which can be ascribed to efficient electron transportation channel and the high utilization rate of the active materials. The anode electrode of hollow sphere α-Fe_2O_3 reveals excellent electrochemical properties with a specific capacitance of 802 F g^{-1} at 1 A g^{-1} and the capacitance retention of 70.3% at the high current density of 16 A g^{-1} which also shows a good rate capability due to the good conductivity and the ability of the hollow spherical structure composed of nanoparticles to efficient transport electron. The PVA&KOH was utilized as the separator and the solid electrolyte of the two all-solid-state ACS devices in series which has been constructed by the cathode electrode of $CoNiO_2$@-NiAl-LDH and the anode electrode of hollow sphere α-Fe_2O_3. The $CoNiO_2$@NiAl-LDH//α-Fe_2O_3 TSASC exhibits a maximum energy density of 65.68 Wh kg^{-1} at the power density of 369.45 W kg^{-1}. Moreover, the system shows an enhanced cycling stability of 88.8% retained over 1000 cycles at the current

density of 1 A g^{-1} which is compared to previously reported ASC devices. Moreover, in addition to many advantages that the solid electrolyte in ASC devices already have, it can be interestingly found that it can be an alternative way of solving the problem of iron oxide cycling performance, and of course it can be analogue to other materials with poor cycling performance.

Abbreviations
ASCs: Asymmetric supercapacitors; CTAB: Hexadecyl trimethyl ammonium bromide; EDLCs: Electrical double-layer capacitors; EDX: Energy dispersive X-ray; EIS: Electrochemical impedance spectroscopy; FESEM: Field emission scanning electron microscopy; HRTEM: High-resolution transmission electron microscopy; NiAl-LDH: NiAl-layered double hydroxide; OLED: Organic light-emitting diode; PSS: Sodium-p-styrenesulfonate; PTFE: Polytetrafluoroethylene; PVA: Polyvinyl alcohol; TEM: Transmission electron microscopy; TLASC: Two liquid ASC devices in series; TSASC: Two solid ASC devices in series; XRD: X-ray diffractometer

Availability of Data and Materials
All data are fully available without restriction.

Authors' Contributions
All authors contributed to the preparation of the manuscript and to the discussion. All authors read and approved the final manuscript.

Competing Interests
The authors declare that they have no competing interests.

Publisher's Note
Springer Nature remains neutral with regard to jurisdictional claims in published maps and institutional affiliations.

References
1. Chen LF, Huang ZH, Liang HW, Guan QF, Yu SH (2013) Bacterial-cellulose-derived carbon nanofiber@ MnO2 and nitrogen-doped carbon nanofiber electrode materials: an asymmetric supercapacitor with high energy and power density. Adv Mater 25(34):4746–4752
2. Fan Z, Yan J, Wei T, Zhi L, Ning G, Li T et al (2011) Asymmetric supercapacitors based on graphene/MnO2 and activated carbon nanofiber electrodes with high power and energy density. Adv Funct Mater 21(12):2366–2375
3. He X, Li R, Liu J, Liu Q, Song D, Wang J (2018) Hierarchical FeCo2O4@ NiCo layered double hydroxide core/shell nanowires for high performance flexible all-solid-state asymmetric supercapacitors. Chem Eng J 334:1573–1583
4. Xu J, Sun Y, Lu M, Wang L, Zhang J, Qian J et al (2018) Fabrication of hierarchical MnMoO4· H2O@ MnO2 core-shell nanosheet arrays on nickel foam as an advanced electrode for asymmetric supercapacitors. Chem Eng J 334:1466–1476
5. Yan J, Fan Z, Sun W, Ning G, Wei T, Zhang Q et al (2012) Advanced asymmetric supercapacitors based on Ni (OH) 2/graphene and porous graphene electrodes with high energy density. Adv Funct Mater 22(12):2632–2641
6. Kong W, Lu C, Zhang W, Pu J, Wang Z (2015) Homogeneous core–shell NiCo 2 S 4 nanostructures supported on nickel foam for supercapacitors. J Mater Chem A 3(23):12452–12460
7. Zhang L, Gu H, Sun H, Cao F, Chen Y, Chen GZ (2018) Molecular level one-step activation of agar to activated carbon for high performance supercapacitors. Carbon 132:573–579
8. Wang C, Hu K, Li W, Wang H, Li H, Zou Y et al (2018) Wearable wire-shaped symmetric supercapacitors based on activated carbon-coated graphite fibers. ACS Appl Mater Interfaces 10(40):34302–34310
9. An KH, Kim WS, Park YS, Moon JM, Bae DJ, Lim SC et al (2001) Electrochemical properties of high-power supercapacitors using single-walled carbon nanotube electrodes. Adv Funct Mater 11(5):387–392
10. Liu C, Yu Z, Neff D, Zhamu A, Jang BZ (2010) Graphene-based supercapacitor with an ultrahigh energy density. Nano Lett 10(12):4863–4868
11. Warren R, Sammoura F, Tounsi F, Sanghadasa M, Lin L (2015) Highly active ruthenium oxide coating via ALD and electrochemical activation in supercapacitor applications. J Mater Chem A 3(30):15568–15575
12. Kim S-I, Lee J-S, Ahn H-J, Song H-K, Jang J-H (2013) Facile route to an efficient NiO supercapacitor with a three-dimensional nanonetwork morphology. ACS Appl Mater Interfaces 5(5):1596–1603
13. Li W, Shao J, Liu Q, Liu X, Zhou X, Hu J (2015) Facile synthesis of porous Mn2O3 nanocubics for high-rate supercapacitors. Electrochim Acta 157:108–114
14. Demarconnay L, Raymundo-Pinero E, Béguin F (2011) Adjustment of electrodes potential window in an asymmetric carbon/MnO2 supercapacitor. J Power Sources 196(1):580–586
15. Meher SK, Rao GR (2011) Ultralayered Co3O4 for high-performance supercapacitor applications. J Phys Chem Lett 115(31):15646–15654
16. Zhang G, Lou XW (2013) General solution growth of mesoporous NiCo2O4 nanosheets on various conductive substrates as high-performance electrodes for supercapacitors. Adv Mater 25(7):976–979
17. Zhang J, Chen Z, Wang Y, Li H (2016) Morphology-controllable synthesis of 3D CoNiO2 nano-networks as a high-performance positive electrode material for supercapacitors. Energy 113:943–948
18. Tang Z, Tang C, Gong H (2012) A high energy density asymmetric supercapacitor from nano-architectured Ni (OH) 2/carbon nanotube electrodes. Adv Funct Mater 22(6):1272–1278
19. Cao L, Xu F, Liang YY, Li HL (2004) Preparation of the novel nanocomposite co (OH) 2/ultra-stable Y zeolite and its application as a supercapacitor with high energy density. Adv Mater 16(20):1853–1857
20. Yulian N, Ruiyi L, Zaijun L, Yinjun F, Junkang L (2013) High-performance supercapacitors materials prepared via in situ growth of NiAl-layered double hydroxide nanoflakes on well-activated graphene nanosheets. Electrochim Acta 94:360–366
21. Cai X, Shen X, Ma L, Ji Z, Xu C, Yuan A (2015) Solvothermal synthesis of NiCo-layered double hydroxide nanosheets decorated on RGO sheets for high performance supercapacitor. Chem Eng J 268:251–259
22. Han J, Dou Y, Zhao J, Wei M, Evans DG, Duan X (2013) Flexible CoAl LDH@ PEDOT core/shell nanoplatelet array for high-performance energy storage. Small 9(1):98–106
23. Huang L, Chen D, Ding Y, Feng S, Wang ZL, Liu M (2013) Nickel–cobalt hydroxide nanosheets coated on NiCo2O4 nanowires grown on carbon fiber paper for high-performance pseudocapacitors. Nano Lett 13(7):3135–3139
24. Liang X, Chen K, Xue D (2018) A flexible and ultrahigh energy density capacitor via enhancing surface/Interface of carbon cloth supported colloids. Adv Energy Mater 8(16):1703329
25. Sun S, Zhai T, Liang C, Savilov SV, Xia H (2018) Boosted crystalline/amorphous Fe2O3-δ core/shell heterostructure for flexible solid-state pseudocapacitors in large scale. Nano Energy 45:390–397
26. Zhao Y, Wang Z, Yuan R, Lin Y, Yan J, Zhang J et al (2018) ZnO/carbon hybrids derived from polymer nanocomposite precursor materials for pseudocapacitor electrodes with high cycling stability. Polymer 137:370–377
27. Yang J, Yu C, Hu C, Wang M, Li S, Huang H et al (2018) Surface-confined fabrication of ultrathin nickel cobalt-layered double hydroxide Nanosheets for high-performance supercapacitors. Adv Funct Mater 28(44):1803272
28. Li H, Musharavati F, Zalenezhad E, Chen X, Hui K, Hui K (2018) Electrodeposited NiCo layered double hydroxides on titanium carbide as a binder-free electrode for supercapacitors. Electrochim Acta 261:178–187
29. Li L, San Hui K, Hui KN, Xia Q, Fu J, Cho Y-R (2017) Facile synthesis of NiAl layered double hydroxide nanoplates for high-performance asymmetric supercapacitor. J Alloy Compd 721:803–812

30. Liu M, He S, Miao Y-E, Huang Y, Lu H, Zhang L et al (2015) Eco-friendly synthesis of hierarchical ginkgo-derived carbon nanoparticles/NiAl-layered double hydroxide hybrid electrodes toward high-performance supercapacitors. RSC Adv 5(68):55109–55118

31. Zhao J, Chen J, Xu S, Shao M, Zhang Q, Wei F et al (2014) Flexible electronics: hierarchical NiMn layered double hydroxide/carbon nanotubes architecture with superb energy density for flexible supercapacitors (Adv. Funct. Mater. 20/2014). Adv Funct Mater 24(20):2921–2921

32. Wan H, Liu J, Ruan Y, Lv L, Peng L, Ji X et al (2015) Hierarchical configuration of NiCo2S4 nanotube@ Ni–Mn layered double hydroxide arrays/three-dimensional graphene sponge as electrode materials for high-capacitance supercapacitors. ACS Appl Mater Interfaces 7(29):15840–15847

33. Yang J, Yu C, Fan X, Qiu J (2014) 3D architecture materials made of NiCoAl-LDH nanoplates coupled with NiCo-carbonate hydroxide nanowires grown on flexible graphite paper for asymmetric supercapacitors. Adv Energy Mater 4(18):1400761

34. Li M, Cheng J, Fang J, Yang Y, Liu F, Zhang X (2014) NiAl-layered double hydroxide/reduced graphene oxide composite: microwave-assisted synthesis and supercapacitive properties. Electrochim Acta 134:309–318

35. Xia H, Meng YS, Yuan G, Cui C, Lu L (2012) A symmetric RuO2/RuO2 supercapacitor operating at 1.6 V by using a neutral aqueous electrolyte. Electrochem Solid-State Lett 15(4):A60–A63

36. Wang H, Xu Z, Yi H, Wei H, Guo Z, Wang X (2014) One-step preparation of single-crystalline Fe2O3 particles/graphene composite hydrogels as high performance anode materials for supercapacitors. Nano Energy 7:86–96

37. Tang X, Jia R, Zhai T, Xia H (2015) Hierarchical Fe3O4@ Fe2O3 core–shell nanorod arrays as high-performance anodes for asymmetric supercapacitors. ACS Appl Mater Interfaces 7(49):27518–27525

38. Chen H-C, Wang C-C, Lu S-Y (2014) γ-Fe 2 O 3/graphene nanocomposites as a stable high performance anode material for neutral aqueous supercapacitors. J Mater Chem A 2(40):16955–16962

39. Zhang Y, Li H, Pan L, Lu T, Sun Z (2009) Capacitive behavior of graphene–ZnO composite film for supercapacitors. J Electroanal Chem 634(1):68–71

40. Zhai T, Lu X, Ling Y, Yu M, Wang G, Liu T et al (2014) A new benchmark capacitance for supercapacitor anodes by mixed-valence sulfur-doped V6O13– x. Adv Mater 26(33):5869–5875

41. Qu Q, Zhu Y, Gao X, Wu Y (2012) Core–shell structure of polypyrrole grown on V2O5 nanoribbon as high performance anode material for supercapacitors. Adv Energy Mater 2(8):950–955

42. Fleischmann S, Zeiger M, Jäckel N, Krüner B, Lemkova V, Widmaier M et al (2017) Tuning pseudocapacitive and battery-like lithium intercalation in vanadium dioxide/carbon onion hybrids for asymmetric supercapacitor anodes. J Mater Chem A 5(25):13039–13051

43. Liu X, Zhang Y, Xia X, Shi S, Lu Y, Wang XL et al (2013) Self-assembled porous NiCo2O4 hetero-structure array for electrochemical capacitor. J Power Sources 239:157–163

44. Li H, Chen Z, Wang Y, Zhang J, Yan X (2016) Controlled synthesis and enhanced electrochemical performance of self-assembled rosette-type Ni-Al layered double hydroxide. Electrochim Acta 210:15–22

45. Gu Z, Zhang X (2016) NiCo 2 O 4@ MnMoO 4 core–shell flowers for high performance supercapacitors. J Mater Chem A 4(21):8249–8254

46. Wang S, Huang Z, Li R, Zheng X, Lu F, He T (2016) Template-assisted synthesis of NiP@ CoAl-LDH nanotube arrays with superior electrochemical performance for supercapacitors. Electrochim Acta 204:160–168

47. Liang H, Lin J, Jia H, Chen S, Qi J, Cao J et al (2018) Hierarchical NiCo-LDH/NiCoP@ NiMn-LDH hybrid electrodes on carbon cloth for excellent supercapacitors. J Mater Chem A 6(31):15040–15046

48. Zhou J-J, Han X, Tao K, Li Q, Li Y-L, Chen C et al (2018) Shish-kebab type MnCo2O4@ Co3O4 nanoneedle arrays derived from MnCo-LDH@ ZIF-67 for high-performance supercapacitors and efficient oxygen evolution reaction. Chem Eng J 354:875–884

49. Ren L, Zhang G, Yan Z, Kang L, Xu H, Shi F et al (2017) High capacitive property for supercapacitor using Fe3+/Fe2+ redox couple additive electrolyte. Electrochim Acta 231:705–712

50. Fan Y, Wang L, Ma Z, Dai W, Shao H, Wang H et al (2018) The in situ synthesis of Fe (OH) 3 film on Fe foam as efficient anode of alkaline supercapacitor based on a promising Fe3+/Fe0 energy storage mechanism. Part Part Syst Charact 35:1700484

51. Zeng YX, Han Y, Zhao YT, Zeng Y, Yu MH, Liu YJ et al (2015) Advanced Ti-doped Fe2O3@PEDOT core/shell anode for high-energy asymmetric supercapacitors. Adv Energy Mater 5(12):1402176

52. Wang Y, Zhang M, Pan D, Li Y, Ma T, Xie J (2018) Nitrogen/sulfur co-doped graphene networks uniformly coupled N-Fe 2 O 3 nanoparticles achieving enhanced supercapacitor performance. Electrochim Acta 266:242–253

53. Song Z, Liu W, Wei W, Quan C, Sun N, Zhou Q et al (2016) Preparation and electrochemical properties of Fe 2 O 3 /reduced graphene oxide aerogel (Fe 2 O 3 /rGOA) composites for supercapacitors. J Alloy Compd 685:355–363

54. Quan H, Cheng B, Xiao Y, Lei S (2016) One-pot synthesis of α-Fe 2 O 3 nanoplates-reduced graphene oxide composites for supercapacitor application. Chem Eng J 286:165–173

55. Gao Y, Wu D, Wang T, Jia D, Xia W, Lv Y et al (2016) One-step solvothermal synthesis of quasi-hexagonal Fe 2 O 3 nanoplates/graphene composite as high performance electrode material for supercapacitor. Electrochim Acta 191:275–283

56. Wang Y, Chen Z, Lei T, Ai Y, Peng Z, Yan X et al (2018) Hollow NiCo2S4 nanospheres hybridized with 3D hierarchical porous rGO/Fe2O3 composites toward high-performance energy storage device. Adv Energy Mater 8:1703453

57. Zhao J, Li Z, Yuan X, Yang Z, Zhang M, Meng A et al (2018) A high-energy density asymmetric supercapacitor based on Fe2O3 nanoneedle arrays and NiCo2O4/Ni (OH) 2 hybrid nanosheet arrays grown on SiC nanowire networks as free-standing advanced electrodes. Adv Energy Mater 8(12):1702787

58. Yang P, Ding Y, Lin Z, Chen Z, Li Y, Qiang P et al (2014) Low-cost high-performance solid-state asymmetric supercapacitors based on MnO2 nanowires and Fe2O3 nanotubes. Nano Lett 14(2):731–736

59. Liang H, Xia C, Emwas A-H, Anjum DH, Miao X, Alshareef HN (2018) Phosphine plasma activation of α-Fe2O3 for high energy asymmetric supercapacitors. Nano Energy 49:155–162

60. Cho S, Patil B, Yu S, Ahn S, Hwang J, Park C et al (2018) Flexible, Swiss roll, fiber-shaped, asymmetric supercapacitor using MnO2 and Fe2O3 on carbon fibers. Electrochim Acta 269:499–508